HHS Public Access

Author manuscript

Ultrasound Med Biol. Author manuscript; available in PMC 2020 September 09.

Published in final edited form as:

Ultrasound Med Biol. 2019 September ; 45(9): 2493–2501. doi:10.1016/j.ultrasmedbio.2019.05.026.

Validation of normalized singular spectrum area as a classifier for molecularly targeted microbubble adherence.

Elizabeth B Herbst, B.Sc.[a], **Sunil Unnikrishnan, Ph.D.**[a], **Alexander L Klibanov, Ph.D.**[a,b], **F William Mauldin Jr., Ph.D.**[a], **John A Hossack, Ph.D.**[a]

[a]Department of Biomedical Engineering, University of Virginia, Charlottesville, VA 22908, USA

[b]Division of Cardiovascular Medicine, University of Virginia, Charlottesville, VA 22908, USA

Abstract

Ultrasound molecular imaging is a diagnostic technique wherein molecularly targeted microbubble contrast agents are imaged to reveal disease markers on the blood vessel endothelium. Currently, microbubble adhesion to affected tissue can be quantified using differential targeted enhancement (dTE), which measures the late enhancement of adherent microbubbles through administration of destructive ultrasound pressures. In this study, we investigate a statistical parameter called normalized singular spectrum area (NSSA) as a means to detect microbubble adhesion without microbubble destruction. We compare the signal differentiation capability of NSSA with matched dTE measurements in a mouse hindlimb tumor model. Results demonstrate that NSSA-based signal classification performance matches dTE when differentiating adherent microbubble from non-adherent microbubble signals (receiver operating characteristic area under the curve = 0.95), and improves classification performance when differentiating microbubble from tissue signals ($p < 0.005$). NSSA-based signal classification eliminates the need for destruction of contrast, and may offer better sensitivity, specificity, and the opportunity for real-time microbubble detection and classification.

Keywords

Ultrasound molecular imaging; microbubbles; differential targeted enhancement; normalized singular spectrum area

INTRODUCTION:

The utility of diagnostic ultrasound imaging is enhanced through the use of contrast agents known as microbubbles (MBs). MBs, typically comprised of a gas core surrounded by a lipid shell, produce a strong acoustic response, which allows for the high-contrast visualization of both blood flow dynamics and vessel wall features in healthy or diseased

Corresponding Author: John A. Hossack, Ph.D., jh7fj@virginia.edu, *Phone:* 434-243-5866, *Address:* 415 Lane Road, N Entrance, Charlottesville, VA 22904.

tissues. In clinical usage, MBs are currently employed for blood volume visualization in left ventricular opacification (Chahal and Senior 2010) or perfusion imaging (Cantisani et al. 2015; Wang et al. 2015c). By attaching ligands to the outside of the MB shell, MBs can be targeted to disease molecular markers expressed on the vascular endothelium, thus revealing, with potentially high sensitivity and specificity, diagnostic information on a molecular scale. This technique, known as ultrasound molecular imaging (USMI), has previously been demonstrated in preclinical studies to detect markers of vascular diseases such as cancer (Bachawal et al. 2013; Barua et al. 2014; Fischer et al. 2010; Wang et al. 2016), atherosclerosis (Kaufmann et al. 2007; Khanicheh et al. 2013; Nitta-Seko et al. 2010), and inflammation (Klibanov et al. 2006; Lindner et al. 2001; Wang et al. 2013a). Recent clinical studies have also utilized USMI for cancer detection and perfusion imaging (Dimcevski et al. 2016; Khong et al. 1999; Smeenge et al. 2017; Wang et al. 2015c; Willmann et al. 2017).

Due to the substantial nonlinear response of MBs, nonlinear imaging techniques such as contrast pulse sequences (CPS) (Phillips 2001), pulse inversion (PI) (Simpson et al. 1999), and other methods (Bouakaz et al. 2002; Forsberg et al. 2000; Needles et al. 2009; Pysz et al. 2012; Zhao et al. 2007) are often employed to suppress tissue signals and enhance MB contrast. However, a known limitation of these nonlinear imaging techniques is the presence of nonlinear artifacts from strongly reflecting tissue structures in the field of view (Tang et al. 2010; Tang and Eckersley 2006). As has been discussed previously (Willmann et al. 2017), these nonlinear artifacts can appear as a false positive signals, which create ambiguity in the final image and often necessitate the manual delineation of the region of interest (ROI) before any nonlinear imaging filter can be applied (Anderson et al. 2010; Fokong et al. 2013; Pysz et al. 2015).

Although non-linear imaging techniques improve overall contrast between MB signals and tissue, these approaches are not intended to differentiate molecularly bound “adherent” MB signals from unbound “free” MBs. Instead, an additional process, referred to as differential targeted enhancement (dTE), may be used to differentiate free from adherent MB signals (Anderson et al. 2011; Bzyl et al. 2011; Deshpande et al. 2011; Ellegala et al. 2003; Lee et al. 2008; Pysz et al. 2015; Rychak et al. 2007a; Turco et al. 2016; Willmann et al. 2008c; Willmann et al. 2008b). Briefly, dTE is used to measure the signal of adherent MBs by calculating the difference between the late enhancement signal (adherent + circulating MBs) and the signal after administration of destructive ultrasound pressures (circulating MBs only). Because a destructive pulse is required, only a single dTE image can be produced per MB injection. The dTE protocols typically necessitate 5–10 min in order to allow for MB binding (Anderson et al. 2011; Bzyl et al. 2011; de Jong et al. 2000; Ellegala et al. 2003; Frinking et al. 2012).

Other studies have sought to measure adherent MB signals via inter-frame image filtering without the need for destruction of contrast. Pysz, *et al* developed an algorithm to separate adherent from non-adherent MB signals based on the dwell time of MBs in a given voxel over a period of 30 s (2012). This method has real-time capability and resulted in greater contrast signal than baseline ultrasound imaging. Zhao, *et al* measured the difference in MB signal before and after the application of acoustic radiation force (ARF), combined with slow-time low-pass filtering, to differentiate free and adherent MB signals from tissue

signals in a large vessel phantom with high sensitivity (2007). This approach was based on MB flow dynamics in large vessels, where acoustic radiation force is often applied to enhance MB binding to the vessel wall (Dayton et al. 1999; Dayton et al. 2002; Rychak et al. 2005; Rychak et al. 2007b; Wang et al. 2013b; Wang et al. 2015b; Wang et al. 2015a; Zhao et al. 2004). However, neither the dwell time nor the low-pass filtering approaches are intended to differentiate MB signals from non-linear tissue leakage artifact signals in small vessel environments, and they tend to accentuate these artifacts, which exhibit the same long dwell times and low temporal frequencies of adherent MBs. Due to these non-linear tissue leakage artifact limitations, ultrasound targeted molecular imaging clinical and pre-clinical studies performed to date have either relied on dTE or manual delineation of the adherent MB regions by an “expert” image interpreter. In clinical studies, researchers have relied primarily upon the late enhancement of adherent MB signals, which does not address nonlinear tissue leakage artifacts and necessitates imaging wait times of up to 30 minutes (Willmann et al. 2017). Because medical ultrasound is often selected clinically due to its bedside and real-time imaging capabilities, limitations of USMI requiring complex protocols and difficult image interpretation may prohibit its adoption.

In contrast to dTE, previous work has demonstrated that an inter-frame signal decorrelation strategy, in combination with ARF, was an effective means of separating nonlinear tissue signals from MB signals with high specificity in a mouse tumor model (Herbst et al. 2017a). This decorrelation-based filtering technique was developed based on the observation that the slow-time signals of both circulating and adherent MBs differ from the slow-time signals of static tissue (Gessner et al. 2009; Needles et al. 2009) (Fig. 1). By creating a filter based on decorrelation between two subsequent imaging frames, effective suppression of nonlinear tissue signals and increased sensitivity to MB signals was achieved.

Previous studies (Wang et al. 2013b) utilized normalized singular spectrum area (NSSA) (Mauldin Jr et al. 2011), a value which is derived from singular value decomposition (SVD) and monotonic with signal decorrelation (Wang et al. 2013b), to differentiate adherent MB signals from non-adherent MB and tissue signals in a large vessel flow phantom. Unlike inter-frame signal decorrelation, which only accounts for variance in the temporal dimension, NSSA-based image filtering exploits the statistical variance of ultrasound signals in both spatial and temporal dimensions (Fig. 2). This allows for more sensitive and specific differentiation between tissue, adherent MB, and free MB signals.

A detailed description of NSSA and singular value-based filtering is described in a previous study (Mauldin Jr et al. 2011). Briefly, NSSA is a measurement characterizing the variability of a matrix based on the non-zero singular values of that matrix. When a matrix is decomposed into left and right singular vectors (U and V, respectively) and a diagonal matrix of singular values (here denoted as S), NSSA is calculated as the sum of S divided by the first singular value of S:

$$NSSA = \frac{\sum_{k}^{N} S_{k,k}}{S_{1,1}}$$

When singular value decomposition is applied to ultrasound data with spatial information in the column dimension and temporal information in the row dimension, NSSA can reveal the spatiotemporal characteristics of adherent MB, non-adherent MB, or static tissue signal. In a matrix that has low dimensionality (e.g. a matrix of static tissue signals), the first singular value has relatively high energy, yielding a low NSSA value. In a matrix containing multi-dimensional information, (e.g. the highly dimensional signal from non-adherent MBs), the energy is dispersed across multiple singular values, yielding a higher NSSA value. In this study, it was hypothesized that NSSA values derived from image regions of adherent MBs are statistically different from NSSA values in image regions of non-adherent MBs in a small-vessel environment.

Experiments were designed to simultaneously acquire NSSA measurements and ground truth dTE measurements from the same imaging sequence in an *in vivo* mouse hindlimb tumor model. Results were collected with both molecularly targeted and isotype control MBs at one minute and six minutes post-injection. Further assessment of results was conducted using receiver operating characteristic (ROC) analysis to quantify the signal classification performance between dTE and NSSA values.

MATERIALS AND METHODS:

1. Microbubble preparation

Microbubbles were prepared in-house using previously described methods (Klibanov et al. 1999; Klibanov et al. 2006). Briefly, biotinylated MBs were formed by sonicating decafluorobutane gas (F2 Chemicals, Lancashire, UK) with a lipid micellar mixture of distearoyl phosphatidylcholine (Avanti Polar Lipids, Alabaster, AL, USA), polyethylene glycol stearate (Stepan Kessco, Elwood, IL, USA) and biotin-PEG3400-distearoylphosphatidylethanolamine (PEG-DSPE, Shearwater Polymers, Huntsville, AL, USA) in normal saline. After MBs were counted using a Coulter Multisizer 3 (Beckman Coulter, Brea, CA, USA) streptavidin (Anaspec Inc, Fremont, CA, USA) was added as a linking molecule at a concentration of 3 μg/10 million microbubbles (Lindner et al. 2001).

MBs were divided into two groups for conjugation to two types of antibodies. The first group was conjugated to biotinylated anti-mouse vascular endothelial growth factor receptor 2 (VEGFR2) antibody (clone Avas 12a1, eBioscience, San Diego, CA, USA) (Lee et al. 2008; Pochon et al. 2010; Willmann et al. 2008c; Willmann et al. 2008a) and the second group was conjugated to biotinylated isotype control antibody (clone R35–95, BD Pharmingen, San Diego, CA, USA). All MBs were conjugated within 48 hours before use. Prior to each experiment, MB concentration was measured using a Coulter Multisizer 3.

2. In vivo mouse hindlimb tumor model

An institutionally approved Animal Care and Use Committee protocol was used for the hindlimb tumor model (Herbst et al. 2017a). Briefly, female C57BL/6 mice were implanted with murine colon adenocarcinoma cells (MC38, Kerafast, Boston, MA, USA) in the hind limb by subcutaneous injection (1×10^6 cells). The implanted tumors were allowed to grow for approximately 7–10 days, or until they reached approximately 1 cm in diameter. On the

day of imaging, mice were anesthetized with 2% isoflurane gas (Henry Schein, Dublin, OH, USA) on a heated motion stage (TM150, Indus Instruments, Webster, TX, USA). After depilation of the affected leg, the tumor was imaged using a Verasonics programmable scanner (Vantage 256; Verasonics, Redmond, WA). For each injection of MBs, phosphate-buffered saline was used to dilute 2×10^7 MBs to a volume of approximately 50 μl, which was then injected via tail vein catheter using a syringe pump (PHD ULTRA, Harvard Apparatus, Holliston, MA, USA) at a rate of approximately 17 μl/min (10^5 MBs/s).

Mice were divided into two groups that received either VEGFR2-targeted or isotype control MBs. Each mouse received two separate injections, with a 10 min waiting period between imaging sessions to allow for MBs to clear. The two injections were used to image MB binding dynamics at two different time points. At each of these two time points, a destruction pulse was administered to obtain a measurement of dTE. Corresponding NSSA measurements were calculated from ensembles of frames collected just before the destruction pulse.

For one of the two injections, dTE and NSSA measurements were collected at 1 min post injection, when it was assumed that MB concentration was high but most MBs (both targeted and non-targeted) were still freely circulating within the tumor. In a separate injection, dTE and NSSA measurements were collected at 6 min post-injection, 5 minutes later than the 1 min time point, when it was assumed that most MBs would be freely circulating (in the case of non-targeted MBs) or adhered to the tumor vasculature (in the case of targeted MBs). The ordering of these two injections was randomized between different mice.

3. Design of imaging sequence

A custom imaging sequence was programmed on a Verasonics ultrasound scanner using a 128-element L12–5 38 mm linear array transducer (Philips Healthcare, Andover, MA). This sequence implemented pulse inversion using a synthetic aperture virtual source element imaging configuration described previously (Herbst et al. 2017a; Wang et al. 2016). Briefly, 22 virtual source elements were defined behind the transducer face and programmed to transmit one positive and one negative amplitude signal (1 cycle, 5.5 MHz). The 44 receive signals (received at 11 MHz) were then compounded to form a final in-phase/quadrature (IQ) frame. Ensembles of these IQ frames through time were then used for NSSA and dTE analysis. The effective frame rate after compounding was 20 Hz.

4. NSSA and dTE measurement

NSSA was calculated from a sliding window of signals that were 5 × 5 × 25 samples, or 0.5 mm × 1 mm × 1.2 s in the axial (fast-time), lateral, and temporal (slow-time) dimension, respectively (Fig. 2). The window was incremented (step size = 1) in the axial and lateral dimensions to create a complete NSSA mapping of one frame occurring just before destruction of contrast (Fig. 3).

For each experiment, an intratumor ROI was manually delineated. To calculate dTE, the mean signal intensity within this ROI was measured before and after MB destruction. To calculate MB NSSA values, the mean NSSA value within the same ROI was measured

immediately before MB destruction. To compare the behavior of MB signals to static tissue signals, a second ROI was selected in a region of static tissue for NSSA and dTE analysis (Fig. 3).

5. Data analysis

Power analysis based on a preliminary study (n = 3) determined that 12 mice in each group (targeted and non-targeted MBs) would yield a statistical power of 0.8 or greater (Herbst et al. 2017b). To isolate the contributions of microbubble and tissue signals, ROIs were chosen in the intratumor space and in regions of highly reflective tissue signals (Fig. 3). This allowed for a one-to-one comparison between ground truth dTE values (measured as the mean pre-burst minus post-burst signal intensity in the ROI) and NSSA values (measured as the mean NSSA value within the same ROI). For both NSSA and dTE measurements, a one-way analysis of variance (ANOVA) and post-hoc multiple comparisons test were used to compare tissue, targeted MB, and non-targeted MB signals (significance level = 0.01). To compare NSSA measurements to ground truth dTE measurements, linear correlation was calculated between NSSA and dTE for all microbubble data sets.

Receiver operating characteristic (ROC) analysis was used to compare the classification performance of the dTE and NSSA measurements. In ROC analysis, the measured area under the curve (AUC) of the false positive rate plotted against the true positive rate is equal to 1.0 for perfect classification, and < 1.0 for imperfect classification. Classification performance was assessed between targeted and non-targeted MB signals at the 6-minute time point, and between tissue and all MB signals at both time points. The AUC of dTE and NSSA ROC curves were compared using a one-tailed Hanley and McNeil method (significance level = 0.01) (1983).

RESULTS:

1. NSSA-based classification of MB signals

To compare the classification accuracy of the two methods, the mean NSSA and dTE values of static tissue, targeted MBs, and non-targeted MBs were evaluated at the 6 min time point. A one-way ANOVA showed a statistically significant difference between the three groups for both dTE ($p < 0.01$) and NSSA ($p < 0.01$) (Fig. 4). A post-hoc multiple comparisons test with Bonferroni correction showed that the NSSA values of targeted and non-targeted MB signals were significantly different at 6 min post-injection ($p < 0.01$), but not at 1 min post-injection ($p = 0.24$). These results agreed with dTE measurements, which showed a statistically significant difference between targeted and non-targeted MB signals at 6 min post-injection ($p < 0.01$) but no significant difference at 1 min post-injection ($p = 0.23$). These results confirmed our hypothesis that NSSA is capable of differentiating between targeted and non-targeted MB signals. NSSA plots of targeted MBs throughout the entire time course of injection showed a gradual decrease of MB NSSA values during binding (Fig. 5).

2. Receiver operating characteristic analysis

The classification performance of dTE and NSSA measurements was evaluated using receiver operating characteristic (ROC) analysis. For separation of targeted from non-targeted MBs (red curves Fig. 6), the measured area under the curve (AUC) was 0.95 for NSSA and 0.95 for dTE. No significant difference was found between the two measurements. For separation of tissue from all MBs at both 1 min and 6 min (blue curves, Fig. 6), the measured area under the curve (AUC) was 1.00 for NSSA and 0.89 for dTE. NSSA demonstrated significantly better classification accuracy than dTE ($p < 0.005$).

3. Correlation between dTE and NSSA

For all trials, the mean intratumoral NSSA value was plotted against the mean dTE within a given ROI (Fig. 7). A linear correlation between mean NSSA and dTE was calculated with an R^2 value of 0.81. The NSSA and dTE values of tissue signals were also plotted (black dots, Fig. 7). Static tissue signals exhibited both low NSSA values and low dTE values.

DISCUSSION:

1. Validation of NSSA for classification of MB signals

Our results demonstrated that NSSA can be used to differentiate between adherent and non-adherent MBs with high sensitivity and specificity. ROC analysis showed that at 6 min post-injection, NSSA measurements matched dTE measurements in classification accuracy between targeted and non-targeted MB signals, and NSSA demonstrated improvements compared to dTE in classifying MB signals against tissue signal (Fig. 6). It was also observed that NSSA of MB signals from all trials had a strong linear correlation with corresponding dTE measurements (Fig. 7). These results suggest that NSSA-based measurement of adherent MB signal may be a viable alternative to dTE-based techniques.

A unique feature of NSSA measurement techniques compared to dTE is that destruction of MBs is not required to measure MB binding. Since NSSA can be measured from the ultrasound image without disruption of MB flow, it provides an opportunity for real-time monitoring of the molecular marker concentration in the tissue region of interest. Furthermore, since NSSA measurements can be captured dynamically from a single injection, the patient requires a lower total dose of contrast agent, thus decreasing the likelihood of adverse events (Spivak et al. 2015; Wang et al. 2016).

One limitation of this study is that all dTE and NSSA measurements are derived from signals within tumor tissue, and therefore, each ROI contains a combination of adherent MB, non-adherent MB, and static tissue signals. The collected dTE and NSSA measurements are therefore not measurements of adherent or non-adherent MB signals alone. A measurement of pure adherent or non-adherent MB signal would require a separate *in vitro* study. However, the purpose of this study was to validate the classification performance of NSSA in a realistic pre-clinical case, where in the case of disease detection, adherent MB signals would be overlaid with both tissue signals and signals from freely circulating MBs.

2. NSSA-based insight into the kinetics of MB binding

Most dTE protocols require acquisition times between 5 and 10 minutes before MB adherence can be measured (Anderson et al. 2011; Bzyl et al. 2011; Ellegala et al. 2003; Frinking et al. 2012). dTE measurements must be acquired in the late phase of MB adhesion, after MBs bind to tissue and most circulating MBs have cleared. When a dTE measurement is collected, it provides a single instantaneous measurement of MB adherence at a single time point. Subsequent dTE measurements require additional injections of contrast.

Because NSSA relies on the combined signals of adherent and circulating MBs, it has the potential to provide information about the binding kinetics of MBs throughout the course of injection. Figure 8 illustrates the NSSA and signal intensity of the intratumoral space after a representative bolus injection of targeted MBs. The NSSA plot indicates that NSSA decreases exponentially during the first 100 s after injection and then remains relatively steady until the destruction phase. This indicates two potential benefits of NSSA-based adherent MB detection: First, it indicates that useful information regarding MB adhesion could be measured, using either dTE or NSSA, as early as 2 minutes after injection, instead of the estimated waiting time of 6 min used for our experiments. Second, the NSSA plot may represent an inverted function of MB adhesion rate (Turco et al. 2017), which would reveal details of MB binding kinetics through time. The NSSA plot may provide more information than a time intensity curve (TIC) alone, which measures the combined signals of adherent and non-adherent MBs. It is demonstrated in Figure 8 that the magnitude of a TIC remains relatively steady for the first few minutes after injection, regardless of the amount of MB binding. A strong understanding of the potential benefits of NSSA-based measurement techniques requires further investigation.

CONCLUSIONS:

In this study, NSSA was validated as a method of differentiation between adherent and non-adherent MB signals in the tumor microvasculature. NSSA achieved the same classification performance as dTE when differentiating adherent and non-adherent MB signals (ROC area under the curve = 0.95), but without the requirement for a destruction pulse. NSSA also demonstrated improvements in performance compared to dTE in differentiating MB signals from tissue signals at any time point measured after injection ($p < 0.005$). The development of an NSSA-based imaging method that can classify MB signals without application of high ultrasound pressures or destruction of the contrast agent may facilitate wider adoption of ultrasound molecular imaging protocols in clinical usage upon positive completion of any necessary trial and regulatory clearance.

ACKNOWLEDGEMENTS:

This study was funded by NIH R01 HL132395. Elizabeth B. Herbst was supported by the NIH Biotechnology Training Program and the University of Virginia Jefferson Fellowship. The authors would like to thank Jeremy Gatesman for his expertise in animal handling.

REFERENCES:

Anderson CR, Hu X, Zhang H, Tlaxca J, Decleves A-E, Houghtaling R, Sharma K, Lawrence M, Ferrara KW, Rychak JJ. Ultrasound molecular imaging of tumor angiogenesis with an integrin targeted microbubble contrast agent. Invest Radiol United States, 2011;46:215–224.

Anderson CR, Rychak JJ, Backer M, Backer J, Ley K, Klibanov AL. scVEGF microbubble ultrasound contrast agents: a novel probe for ultrasound molecular imaging of tumor angiogenesis. Invest Radiol 2010;45:579–85. [PubMed: 20733505]

Bachawal SV, Jensen KC, Lutz AM, Gambhir SS, Tranquart F, Tian L, Willmann JK. Earlier detection of breast cancer with ultrasound molecular imaging in a transgenic mouse model. Cancer Res 2013;73:1689–1698. [PubMed: 23328585]

Barua A, Yellapa A, Bahr JM, Machado SA, Bitterman P, Basu S, Sharma S, Abramowicz JS. Enhancement of ovarian tumor detection with alphavbeta3 integrin-targeted ultrasound molecular imaging agent in laying hens: a preclinical model of spontaneous ovarian cancer. Int J Gynecol Cancer United States, 2014;24:19–28.

Bouakaz A, Frigstad S, Ten Cate FJ, de Jong N. Super harmonic imaging: A new imaging technique for improved contrast detection. Ultrasound Med Biol 2002;28:59–68. [PubMed: 11879953]

Bzyl J, Lederle W, Rix A, Grouls C, Tardy I, Pochon S, Siepmann M, Penzkofer T, Schneider M, Kiessling F, Palmowski M. Molecular and functional ultrasound imaging in differently aggressive breast cancer xenografts using two novel ultrasound contrast agents (BR55 and BR38). Eur Radiol 2011;21:1988–1995. [PubMed: 21562807]

Cantisani V, Bertolotto M, Weskott HP, Romanini L, Grazhdani H, Passamonti M, Drudi FM, Malpassini F, Isidori A, Meloni FM, Calliada F, D'ambrosio F. Growing indications for CEUS: The kidney, testis, lymph nodes, thyroid, prostate, and small bowel. Eur J Radiol 2015;

Chahal NS, Senior R. Clinical Applications of Left Ventricular Opacification. JACC Cardiovasc Imaging 2010;3:188–196. [PubMed: 20159646]

Dayton P, Klibanov A, Brandenburger G, Ferrara K. Acoustic radiation force in vivo: a mechanism to assist targeting of microbubbles. Ultrasound Med Biol Elsevier, 1999;25:1195–1201.

Dayton PA, Allen JS, Ferrara KW. The magnitude of radiation force on ultrasound contrast agents. J Acoust Soc Am ASA, 2002;112:2183–2192.

de Jong N, Frinking PJ, Bouakaz A, Ten Cate FJ. Detection procedures of ultrasound contrast agents. Ultrasonics 2000;38:87–92. [PubMed: 10829635]

Deshpande N, Ren Y, Foygel K, Rosenberg J, Willmann JK. Tumor angiogenic marker expression levels during tumor growth: longitudinal assessment with molecularly targeted microbubbles and US imaging. Radiology United States, 2011;258:804–811.

Dimcevski G, Kotopoulis S, Bjånes T, Hoem D, Schjøt J, Gjertsen BT, Biermann M, Molven A, Sorbye H, McCormack E, Postema M, Gilja OH. A human clinical trial using ultrasound and microbubbles to enhance gemcitabine treatment of inoperable pancreatic cancer. J Control Release 2016;

Ellegala DB, Leong-Poi H, Carpenter JE, Klibanov AL, Kaul S, Shaffrey ME, Sklenar J, Lindner JR. Imaging tumor angiogenesis with contrast ultrasound and microbubbles targeted to alpha(v)beta3. Circulation United States, 2003;108:336–341.

Fischer T, Thomas A, Tardy I, Schneider M, Hünigen H, Custodis P, Beyersdorff D, Plendl J, Schnorr J, Diekmann F, Gemeinhardt O. Vascular endothelial growth factor receptor 2-specific microbubbles for molecular ultrasound detection of prostate cancer in a rat model. Invest Radiol 2010;45:675–684. [PubMed: 20733504]

Fokong S, Fragoso A, Rix A, Curaj A, Wu Z, Lederle W, Iranzo O, Gätjens J, Kiessling F, Palmowski M. Ultrasound molecular imaging of E-selectin in tumor vessels using poly n-butyl cyanoacrylate microbubbles covalently coupled to a short targeting peptide. Invest Radiol 2013;48:843–50. [PubMed: 23857137]

Forsberg F, Shi WT, Goldberg BB. Subharmonic imaging of contrast agents. Ultrasonics 2000;38:93–98. [PubMed: 10829636]

Frinking PJA, Tardy I, Theraulaz M, Arditi M, Powers J, Pochon S, Tranquart F. Effects of acoustic radiation force on the binding efficiency of BR55, a VEGFR2-specific ultrasound contrast agent. Ultrasound Med Biol England, 2012;38:1460–1469.

Gessner R, Lukacs M, Lee M, Tsuruta J, Foster FS, Dayton PA. Radiation force-enhanced targeted imaging and near real-time molecular imaging using a dual-frequency high-resolution transducer: In-vitro and in-vivo results. Proc - IEEE Ultrason Symp 2009.

Hanley JA, McNeil BJ. A method of comparing the areas under receiver operating characteristic curves derived from the same cases. Radiology 1983;

Herbst EB, Unnikrishnan S, Wang S, Klibanov AL, Hossack JA, Mauldin FW. The Use of Acoustic Radiation Force Decorrelation-Weighted Pulse Inversion for Enhanced Ultrasound Contrast Imaging. Invest Radiol 2017a;52:95–102. [PubMed: 27495188]

Herbst EB, Wang S, Klibanov AL, Mauldin FW, Hossack JA. Microbubble signal classification using normalized singular spectrum area based filtering methods. IEEE Int Ultrason Symp IUS 2017b.

Kaufmann BA, Sanders JM, Davis C, Xie A, Aldred P, Sarembock IJ, Lindner JR. Molecular imaging of inflammation in atherosclerosis with targeted ultrasound detection of vascular cell adhesion molecule-1. Circulation 2007;116:276–284. [PubMed: 17592078]

Khanicheh E, Qi Y, Xie A, Mitterhuber M, Xu L, Mochizuki M, Daali Y, Jaquet V, Krause K-H, Ruggeri ZM, Kuster GM, Lindner JR, Kaufmann B a. Molecular imaging reveals rapid reduction of endothelial activation in early atherosclerosis with apocynin independent of antioxidative properties. Arterioscler Thromb Vasc Biol 2013;33:2187–92. [PubMed: 23908248]

Khong PL, Chau MT, Fan ST, Leong LL. Ultrasound contrast agent Levovist in colour Doppler sonography of hepatocellular carcinoma in Chinese patients. Australas Radiol 1999;43:156–159. [PubMed: 10901894]

Klibanov AL, Hughes MS, Villanueva FS, Jankowski RJ, Wagner WR, Wojdyla JK, Wible JH, Brandenburger GH. Targeting and ultrasound imaging of microbubble-based contrast agents. Magn Reson Mater Physics, Biol Med 1999;8:177–184.

Klibanov AL, Rychak JJ, Yang WC, Alikhani S, Li B, Acton S, Lindner JR, Ley K, Kaul S. Targeted ultrasound contrast agent for molecular imaging of inflammation in high-shear flow. Contrast Media Mol Imaging Wiley Online Library, 2006;1:259–266.

Lee DJ, Lyshchik A, Huamani J. Relationship between retention of a vascular endothelial growth factor receptor 2 (VEGFR2)-targeted ultrasonographic contrast agent and the level of VEGFR2 expression in an in vivo breast cancer model. J Ultrasound Med 2008;2:855–866.

Lindner JR, Song J, Christiansen J, Klibanov AL, Xu F, Ley K. Ultrasound assessment of inflammation and renal tissue injury with microbubbles targeted to P-selectin. Circulation Am Heart Assoc, 2001;104:2107–2112.

Mauldin FW Jr, Lin D, Hossack JA. The singular value filter: a general filter design strategy for PCA-based signal separation in medical ultrasound imaging. IEEE Trans Med Imaging IEEE, 2011;30:1951–1964.

Needles A, Couture O, Foster FS. A method for differentiating targeted microbubbles in real time using subharmonic micro-ultrasound and interframe filtering. Ultrasound Med Biol 2009;35:1564–1573. [PubMed: 19632763]

Nitta-Seko A, Nitta N, Shiomi M, Sonoda A, Ota S, Tsuchiya K, Takahashi M, Fujimiya M, Kiyoshi M. Utility of contrast-enhanced ultrasonography for qualitative imaging of atherosclerosis in Watanabe heritable hyperlipidemic rabbits: initial experimental study. Jpn J Radiol 2010;28:656–662. [PubMed: 21113749]

Phillips PJ. Contrast pulse sequences (CPS): imaging nonlinear microbubbles. IEEE Int Ultrason Symp 2001;1739–1745.

Pochon S, Tardy I, Bussat P, Bettinger T, Brochot J, Von Wronski M, Passantino L, Schneider M. BR55: a lipopeptide-based VEGFR2-targeted ultrasound contrast agent for molecular imaging of angiogenesis. Invest Radiol Lippincott Williams & Wilkins, 2010;45:89–95.

Pysz MA, Guracar I, Tian L, Willmann JK. Fast microbubble dwell-time based ultrasonic molecular imaging approach for quantification and monitoring of angiogenesis in cancer. Quant Imaging Med Surg 2012;2:68–80. [PubMed: 22943043]

Pysz MA, Machtaler SB, Seeley ES, Lee JJ, Brentnall TA, Rosenberg J, Tranquart F, Willmann JK. Vascular endothelial growth factor receptor type 2-targeted contrast-enhanced US of pancreatic cancer neovasculature in a genetically engineered mouse model: potential for earlier detection. Radiology 2015;274:790–799. [PubMed: 25322341]

Rychak JJ, Graba J, Cheung AMY, Mystry BS, Lindner JR, Kerbel RS, Foster FS. Microultrasound molecular imaging of vascular endothelial growth factor receptor 2 in a mouse model of tumor angiogenesis. Mol Imaging 2007a;6:289–296. [PubMed: 18092513]

Rychak JJ, Klibanov AL, Hossack JA. Acoustic radiation force enhances targeted delivery of ultrasound contrast microbubbles: in vitro verification. IEEE Trans Ultrason Ferroelectr Freq Control IEEE, 2005;52:421–433.

Rychak JJ, Klibanov AL, Ley KF, Hossack JA. Enhanced targeting of ultrasound contrast agents using acoustic radiation force. Ultrasound Med Biol 2007b;33:1132–1139. [PubMed: 17445966]

Simpson DH, Chin CT, Burns PN. Pulse inversion Doppler: a new method for detecting nonlinear echoes from microbubble contrast agents. IEEE Trans Ultrason Ferroelectr Freq Control 1999;46:372–82. [PubMed: 18238434]

Smeenge M, Tranquart F, Mannaerts CK, de Reijke TM, van de Vijver MJ, Laguna MP, Pochon S, de la Rosette JJMCH, Wijkstra H. First-in-Human Ultrasound Molecular Imaging With a VEGFR2-Specific Ultrasound Molecular Contrast Agent (BR55) in Prostate Cancer: A Safety and Feasibility Pilot Study. Invest Radiol 2017;52:419–427. [PubMed: 28257340]

Spivak I, Rix A, Schmitz G, Fokong S, Iranzo O, Lederle W, Kiessling F. Low-dose molecular ultrasound imaging with E-selectin-targeted PBCA microbubbles. Mol Imaging Biol 2015;18:180–190.

Tang MX, Eckersley RJ. Nonlinear propagation of ultrasound through microbubble contrast agents and implications for imaging. IEEE Trans Ultrason Ferroelectr Freq Control 2006;

Tang MX, Kamiyama N, Eckersley RJ. Effects of Nonlinear Propagation in Ultrasound Contrast Agent Imaging. Ultrasound Med Biol 2010;

Turco S, El Kaffas A, Zhou J, Wijkstra H, Willmann JK, Mischi M. Quantitative ultrasound molecular imaging for antiangiogenic therapy monitoring. IEEE Int Ultrason Symp IUS 2016.

Turco S, Tardy I, Frinking P, Wijkstra H, Mischi M. Quantitative ultrasound molecular imaging by modeling the binding kinetics of targeted contrast agent. Phys Med Biol 2017;

Wang H, Machtaler S, Bettinger T, Lutz AM, Luong R, Bussat P, Gambhir SS, Tranquart F, Tian L, Willmann JK. Molecular imaging of inflammation in inflammatory bowel disease with a clinically translatable dual-selectin-targeted US contrast agent: comparison with FDG PET/CT in a mouse model. Radiology 2013a;267:818–829. [PubMed: 23371306]

Wang S, Herbst EB, Mauldin FWJ, Diakova GB, Klibanov AL, Hossack JA. Ultra-low-dose ultrasound molecular imaging for the detection of angiogenesis in a mouse murine tumor model: How little can we see? Invest Radiol 2016;51:758–766. [PubMed: 27654582]

Wang S, Mauldin FW, Klibanov AL, Hossack JA. Ultrasound-Based Measurement of Molecular Marker Concentration in Large Blood Vessels: A Feasibility Study. Ultrasound Med Biol 2015a;41:222–234. [PubMed: 25308943]

Wang S, Mauldin FW Jr, Klibanov AL, Hossack JA. Shear forces from flow are responsible for a distinct statistical signature of adherent microbubbles in large vessels. Mol Imaging 2013b;12:1–13.

Wang S, Wang CY, Unnikrishnan S, Klibanov AL, Hossack JA, Mauldin FW. Optical verification of microbubble response to acoustic radiation force in large vessels with in vivo results. Invest Radiol 2015b;50:772–784. [PubMed: 26135018]

Wang X, Yu Z, Guo R, Yin H, Hu X. Assessment of postoperative perfusion with contrast-enhanced ultrasonography in kidney transplantation. Int J Clin Exp Med 2015c;.

Willmann JK, Bonomo L, Carla Testa A, Rinaldi P, Rindi G, Valluru KS, Petrone G, Martini M, Lutz AM, Gambhir SS. Ultrasound Molecular Imaging With BR55 in Patients With Breast and Ovarian Lesions: First-in-Human Results. J Clin Oncol 2017;35:2133–2140. [PubMed: 28291391]

Willmann JK, Cheng Z, Davis C, Lutz AM, Schipper ML, Nielsen CH, Gambhir SS. Targeted microbubbles for imaging tumor angiogenesis: assessment of whole-body biodistribution with dynamic micro-PET in mice. Radiology 2008a;249:212–219. [PubMed: 18695212]

Willmann JK, Lutz AM, Paulmurugan R, Patel MR, Chu P, Rosenberg J, Gambhir SS. Dual-targeted contrast agent for US assessment of tumor angiogenesis in vivo. Radiology 2008b;248:936–944. [PubMed: 18710985]

Willmann JK, Paulmurugan R, Chen K, Gheysens O, Rodriguez-Porcel M, Lutz AM, Chen IY, Chen X, Gambhir SS. US imaging of tumor angiogenesis with microbubbles targeted to vascular endothelial growth factor receptor type 2 in mice. Radiology 2008c;246:508–518. [PubMed: 18180339]

Zhao S, Borden M, Bloch SH, Kruse D, Ferrara KW, Dayton PA. Radiation-force assisted targeting facilitates ultrasonic molecular imaging. Mol Imaging NIH Public Access, 2004;3:135–148.

Zhao S, Kruse DE, Ferrara KW, Dayton PA. Selective imaging of adherent targeted ultrasound contrast agents. Phys Med Biol 2007;52:2055–2072. [PubMed: 17404455]

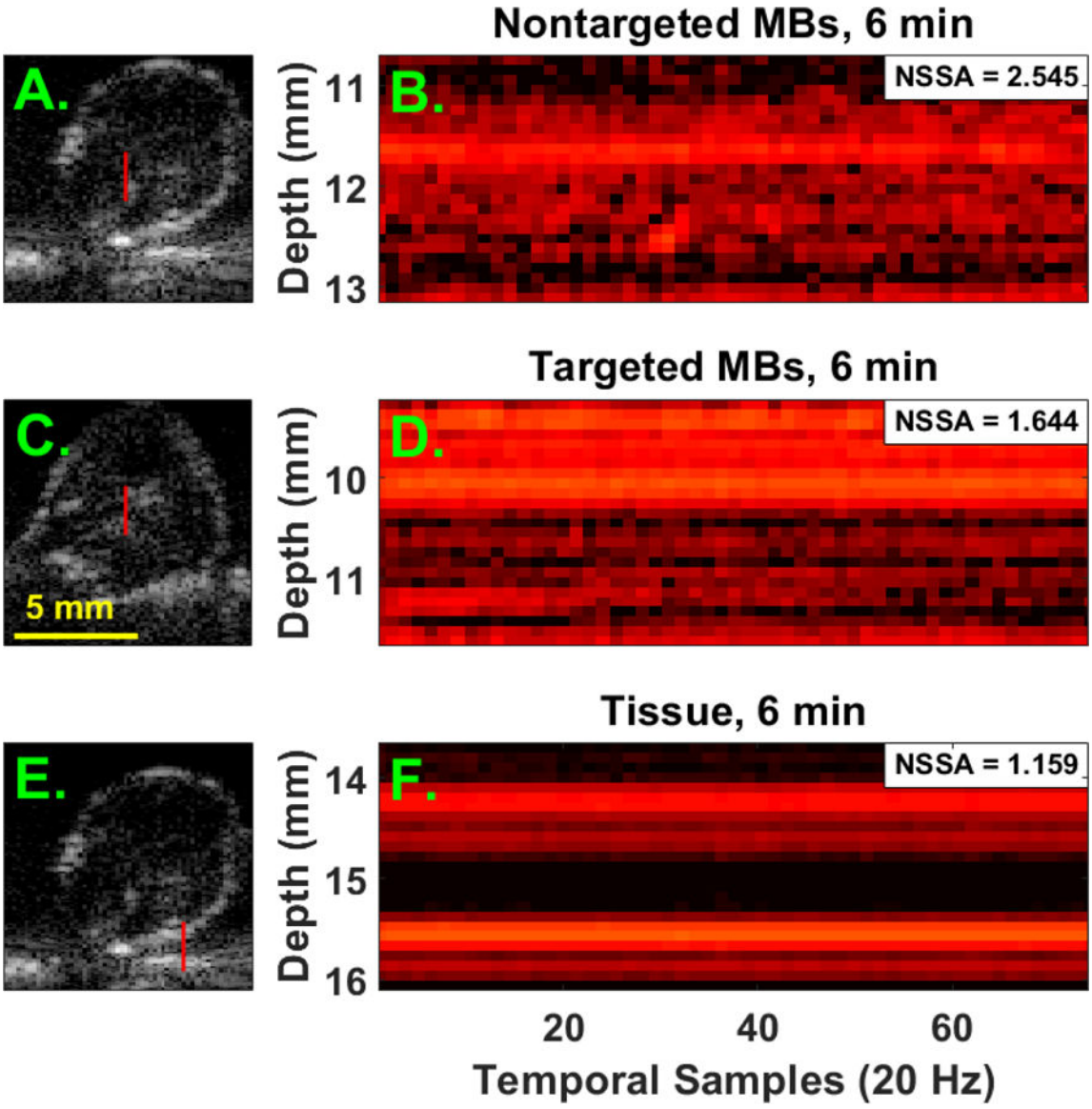

Figure 1. Non-adherent microbubbles, adherent microbubbles, and static tissue exhibit different slow-time characteristics.

M-mode images are displayed to show the change in microbubble (MB) and tissue signals through time (Dynamic range: 50 dB). **A, B:** Highly decorrelated signal from non-adherent MBs results in high variance in the temporal (slow-time) dimension and a high normalized singular spectrum area (NSSA) value. **C, D:** Adherent MB signals exhibit lower variance in the temporal dimension than non-adherent MB signals, thus NSSA is reduced. **E, F:** Static tissue signal has the lowest variance in the temporal dimension, thus its corresponding NSSA measurement is near its minimum possible value of 1.0.

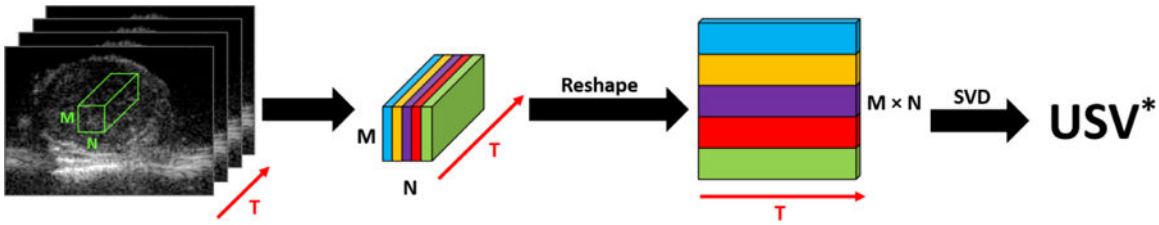

Figure 2. Schematic of image processing algorithm to extract NSSA from an ensemble of ultrasound frames.

3D samples of in-phase/quadrature (IQ) data are rearranged for singular value decomposition (SVD) analysis, followed by calculation of NSSA.

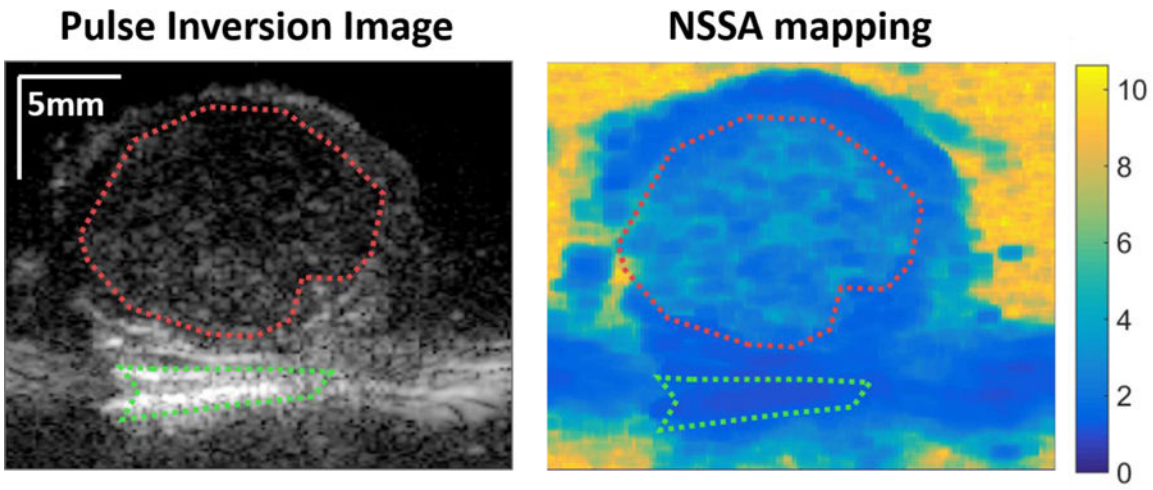

Figure 3. Selection of regions of interest for measurement of tissue and microbubble differential targeted enhancement (dTE) and NSSA.

Red dotted lines show delineation of the intratumor MB signal, measured at either 1 min or 6 min post-injection. Green dotted lines show delineation of the static tissue signal.

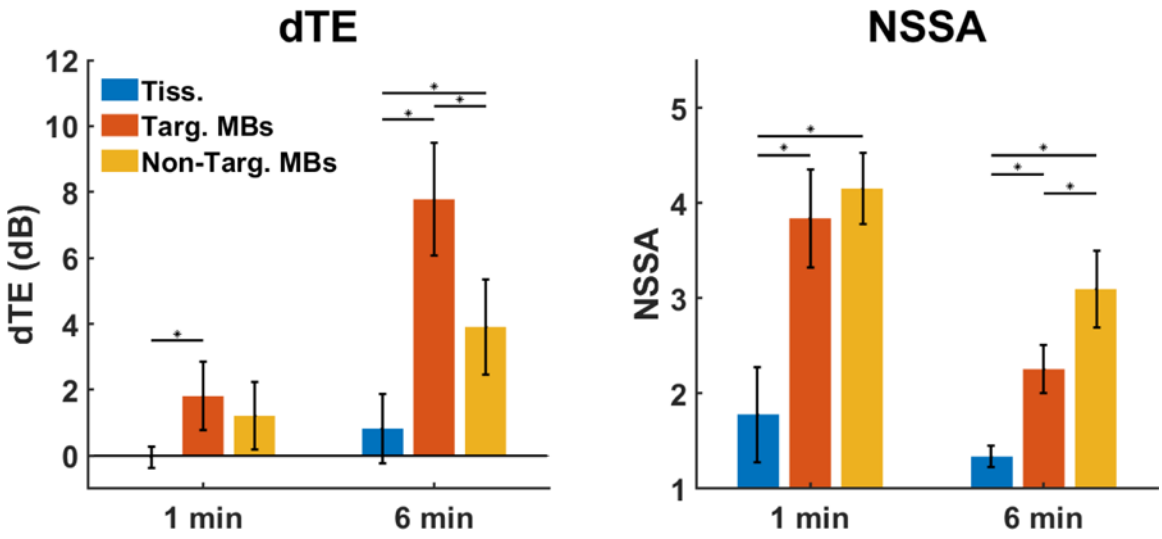

Figure 4. Mean dTE and NSSA values of tissue, targeted microbubble, and non-targeted microbubble signals at 1 min and 6 min post-injection.

A one-way analysis of variance (ANOVA) showed a statistically significant difference between the three groups for both classification techniques. NSSA-based classification allowed for statistically significant separation between targeted and non-targeted MBs at the 6 min time point.

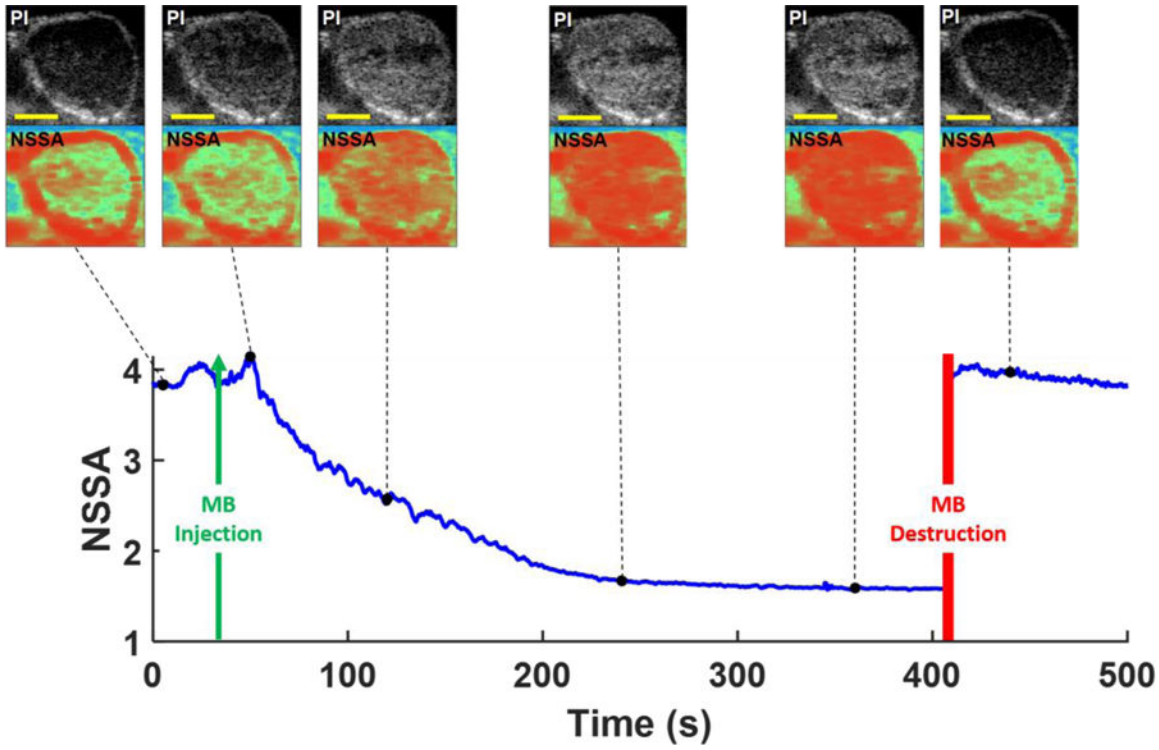

Figure 5. Pulse inversion image and NSSA mapping of the tumor at different time points during targeted microbubble injection, combined with plot of mean MB NSSA signal.

NSSA mappings show that the mean NSSA of targeted MB signals changes gradually throughout the time course of injection and binding. A plot of the mean NSSA signal within a manually chosen intratumoral ROI shows the changes in NSSA during the course of MB injection. Scale bar: 5 mm.

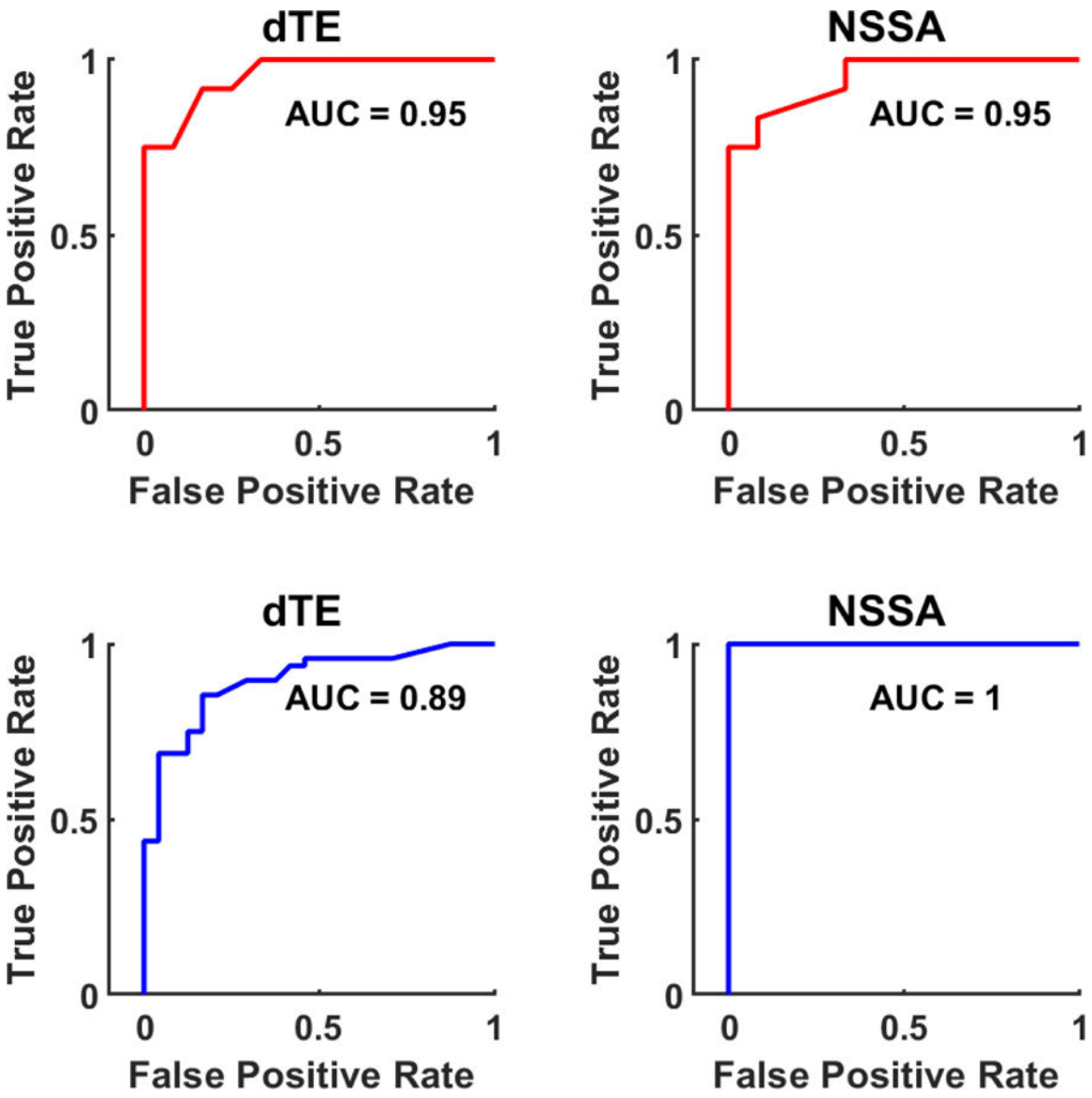

Figure 6. Receiver operating characteristic (ROC) analysis of dTE and NSSA.

ROC analysis for separation of targeted and non-targeted MB signals is shown in red. ROC analysis for separation of tissue signals from all MB signals is shown in blue.

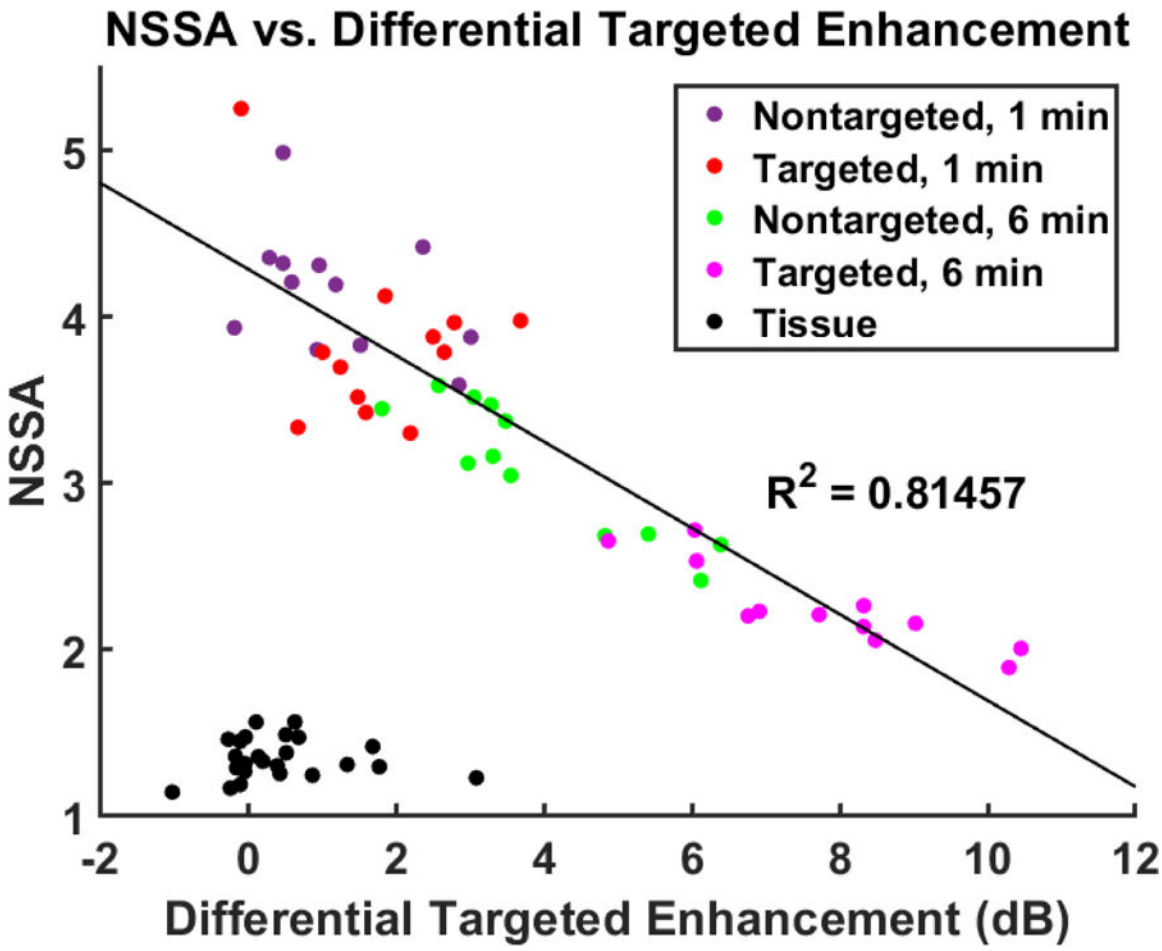

Figure 7. Linear relationship between dTE and NSSA.

MB signals are plotted from each time point (1 min and 6 min post-injection) and each type of MB (targeted and non-targeted) in the experiments. NSSA and dTE measurements of static tissue signal are also plotted (black dots).

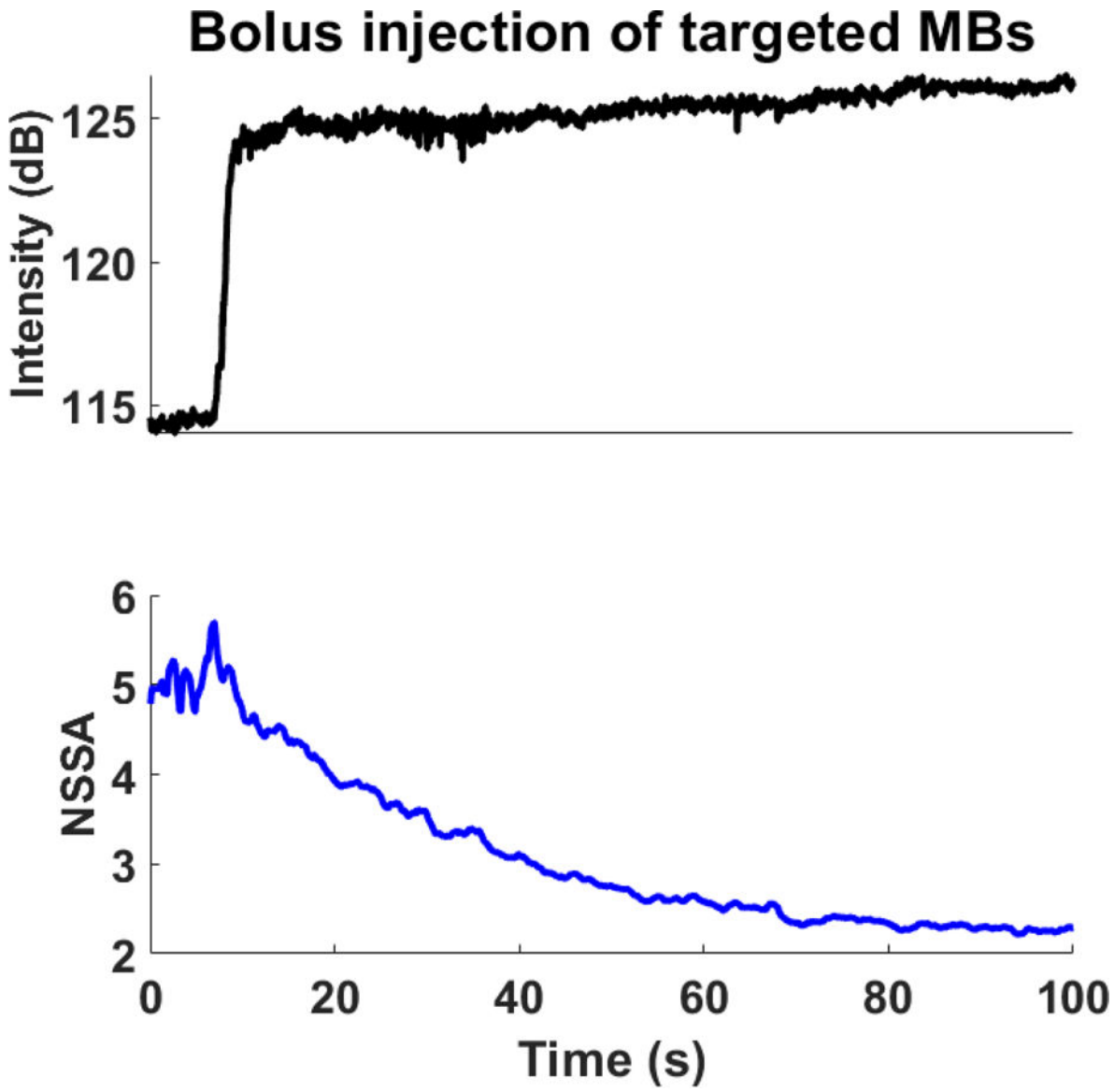

Figure 8. Plots of targeted MB signal intensity and NSSA values during the first 100 s of injection.

Mean MB NSSA and signal intensity values were chosen based on manually delineated intratumoral ROIs (Fig. 3).